Journal of Power Sources 542 (2022) 231775

Contents lists available at ScienceDirect

Journal of Power Sources

journal homepage: www.elsevier.com/locate/jpowsour

Correlative electrochemical acoustic time-of-flight spectroscopy and X-ray imaging to monitor the performance of single-crystal and polycrystalline NMC811/Gr lithium-ion batteries

H. Michael [a,b], R.E. Owen [a,b], J.B. Robinson [a,b], T.M.M. Heenan [a,b], C. Tan [a,b], A.J. Wade [a,b], R. Jervis [a,b], D.J.L. Brett [a,b], P.R. Shearing [a,b,*]

[a] The Electrochemical Innovation Lab, Department of Chemical Engineering, University College London, WC1E 7JE, United Kingdom
[b] The Faraday Institution, Quad One, Harwell Science and Innovation Campus, Didcot, OX11 0RA, UK

HIGHLIGHTS

- Acoustic testing can detect lithium-ion cell degradation during cycling.
- Acoustic behaviour of lithium-ion cells is influenced by electrode morphology.
- Battery performance is affected by electrode morphology.
- X-ray imaging can inform acoustic interpretation of lithium-ion cells.

ARTICLE INFO

Keywords:
NMC
Single crystal
Polycrystalline
Time-of-Flight
X-ray computed tomography

ABSTRACT

$LiNi_xMn_yCo_zO_2$ (NMC) electrodes typically consist of anisotropic single-crystal primary particles aggregated to form polycrystalline secondary particles. Electrodes composed of polycrystalline NMC particles have a comparatively high gravimetric capacity and good rate capabilities but do not perform as well as single crystal equivalents in terms of volumetric energy density and cycling stability. This has prompted research into well-dispersed single-crystalline NMC products as an alternative solution for high-energy-density batteries. Here, for the first time known to the authors, electrochemical acoustic time-of-flight (EA-ToF) spectroscopy has been shown to be effective in distinguishing between Li-ion batteries composed of either single-crystal NMC811 (SC-NMC811) or polycrystalline NMC811 (PC-NMC811) electrodes. Cells composed of PC-NMC811 electrodes had a higher degree of gas evolution compared to cells containing SC-NMC811 electrodes. Cells composed of PC-NMC811 electrodes also underwent larger changes in the acoustic signal's time-of-flight (ToF) during constant current cycling at a range of C-rates indicating expansion, fracture or dislocation of the reflective interfaces inside the cell. In addition, X-ray computed tomography (X-ray CT) has been used to confirm significant morphological differences between SC-NMC811 electrodes and PC-NMC811 electrodes including the electrode's particle size distribution (PSD) that is suggested to have an effect on acoustic signal interaction with these electrode interfaces.

1. Introduction

Li-ion batteries (LiBs) have become ubiquitous in modern life due to their use in an array of applications ranging from consumer electronics, to domestic appliances and electric vehicles (EVs) [1]. While the ever-increasing market share of EVs will inevitably aid the transition to a low carbon future, it is imperative that the batteries used are affordable, can withstand fast-charging and can maintain high capacities for long-distance use. The range of an EV is determined by the energy of the Li-ion cell (and subsequently the battery pack), which is highly dependent on the electrode chemistry and operating conditions. In commercial applications, the cathode is most critical to cell capacity and therefore battery electric vehicle (BEV) range [2].

Many layered transition metal cathodes have been developed and a

* Corresponding author. The Electrochemical Innovation Lab, Department of Chemical Engineering, University College London, WC1E 7JE, United Kingdom.
E-mail address: p.shearing@ucl.ac.uk (P.R. Shearing).

https://doi.org/10.1016/j.jpowsour.2022.231775
Received 7 February 2022; Received in revised form 27 May 2022; Accepted 18 June 2022
Available online 8 July 2022

wide range of $LiNi_xMn_yCo_zO_2$ (NMC) chemistries are currently used in LiBs. They have been deployed in electric and hybrid-electric vehicles and are amongst the most promising LiB cathodes because their layered structures provide higher reversible capacities (>200 mAh g^{-1}) and favourable rate capabilities (electronic conductivity $\approx 2.8 \times 10^{-5}$ S cm^{-1} and Li^+ diffusivity of 10^{-8} to 10^{-9} cm^2 s^{-1}) than previously commercialised $LiCoO_2$ (LCO) cathodes to enable longer-range operation and faster-charging [2]. The NMC particles' crystallinity and morphology has a large influence on the energy density, cycling stability, and rate capability of the electrode in practical applications. For instance, the evolution of micro-cracks in NMC811 (where $x \approx 0.8$) is far more prevalent in polycrystalline NMC811 (PC-NMC811) particles compared to single crystal NMC811 (SC-NMC811) particles, due to an unconstrained expansion in SC-NMC811 particles which lowers the risk of intergranular microcrack formation [2,3]. Though both materials are composed of crystallites of the same material (NMC811 with R3m symmetry), the morphology of these crystallites, and the particles they form, are significantly different. The PC-NMC811 electrode is made up of large (~10 μm), spherical agglomerates of multiple small crystallites of around ~300–500 nm, each of which tends to have an oblong or anisotropic morphology. In contrast, the SC-NMC811 electrode is made up of individual particles of ostensibly single crystallites that are larger than the primary particles, but smaller than their agglomerates in the PC-NMC811 electrode. These particles are of the order of 1–5 μm in size, less oblong in shape and are composed of one, or only a few, crystal grains [4].

In recent years, there has been a move towards the application of new characterisation techniques on batteries to better understand the degradation processes and extend their lifetimes. Of these, acoustic techniques have increased in popularity extremely rapidly [5], with electrochemical acoustic time-of-flight (EA-ToF) spectroscopy being used to study various degradation phenomena in LiBs such as gas formation [6], cell stiffness [7], and cathode dissolution [8]. Electrochemical acoustic time-of-flight (EA-ToF) spectroscopy involves passing an ultrasonic pulse (acoustic signal) through a sample and recording the reflected signal that passes though the sample's respective layers. EA-ToF spectroscopy was first carried out on a battery system by Hsieh et al. to examine the state of health (SoH) of $LiCoO_2$/graphite pouch cells [9]. The key parameter obtained from this type of acoustic experiment is the acoustic time-of-flight (ToF). ToF can be calculated using Eq. (1):

$$ToF = \frac{L}{C_s} = \frac{L}{\sqrt{\frac{E}{\rho}}} \tag{1}$$

where L is the path length travelled, E is the elastic modulus, and ρ is the density of the material. The square root of E/ρ is the speed of sound, C_s, through a given medium [10]. The operating principles of electrochemical acoustic time-of-flight spectroscopy have recently been described elsewhere [5,6,8].

Studies have also commonly coupled EA-ToF spectroscopy with complementary characterisation tools including X-ray diffraction (XRD) [11] and X-ray computed tomography (X-ray CT) [6,8] to further enhance the understanding of structural changes taking place in these materials and architectural changes at the device level [6]. It is widely acknowledged that there are multiple degradation mechanisms at play in the ageing of a LiB and enabling the prediction of which mechanism - or combination of mechanisms - is most critical in particular conditions is vital to understanding and mitigating degradation, particularly for ostensibly similar cells [12,13]. In particular, progress in EA-ToF investigations of LiB material property changes can improve the mechanistic understanding of structural changes during charge/discharge and provide a greater understanding of these LiB dynamics, something which will help to overcome limitations in current density, battery lifetime and capacity fade and ultimately minimise the total cost of battery systems. In addition, EA-ToF spectroscopy is a non-invasive, non-destructive operando technique that can be applied to batteries with minimal cost and high time-resolution results, making it an attractive proposition for detailed on-board diagnostics of operating batteries [10,14]. Whilst X-ray CT is a valuable diagnostic tool for capturing images of LiBs before and after cycling, it is impractical and expensive to carry out large scale cycling of cells inside an X-ray CT instrument for a long period of time; however, many significant findings from lab-based X-ray CT experiments have emerged in recent years related to the link between microstructure and performance, cracking and cell-level failure, amongst others [15–18].

During prolonged cycling, EA-ToF spectroscopy measurements of whole cell assemblies can be complicated by various phenomena including gas formation, material stress changes and thermal expansion. In addition, intrinsic physical properties such as particle size, electrode density, local electrode composition and tortuosity provide significant challenges to directly measuring thicknesses in LiBs, as these factors can vary considerably between different cells and influence their acoustic behaviour. Therefore, some familiarity with the acoustic signature of different full cells is beneficial for discerning changes in acoustic signatures due to intrinsic physical properties and structural changes during cycling.

In this study, correlative X-ray CT was used alongside EA-ToF spectroscopy to provide new insights into how varying the crystallinity of the cathode effects the acoustic behaviour of LiBs. To the authors' knowledge, this is the first time EA-ToF spectroscopy has been carried out on LiBs composed of SC-NMC811 cathodes, to explore whether EA-ToF spectroscopy can provide a sensitivity capable of detecting the intrinsic difference in bulk electrode properties caused by the different particle morphology of the tested NMC811 electrodes. EA-ToF spectroscopy was also used to evaluate changes in the acoustic signal's ToF between LiBs composed of either SC-NMC811 electrodes or PC-NMC811 electrodes during cycling and whether these ToF changes correlated with changes in exterior cell temperature. X-ray CT was used to ascertain the cell assembly parameters and arrangement, to inform the acoustic interpretation. In addition, X-ray nano computed tomography (nano-CT) was used to further understand differences in morphology between SC-NMC811 and PC-NMC811 electrodes that can cause differing acoustic signal interactions and thus influence the acoustic signature of SC-NMC811/Gr and PC-NMC811/Gr cells.

2. Experimental methodology

LiBs comprising NMC811 and graphite electrodes were supplied by LiFUN Technology Ltd (Zhuzhou City, China) in a 5-layer wounded pouch cell configuration with dimensions of 30 mm × 20 mm. The NMC811 and graphite electrodes were fabricated at LiFUN Technology Ltd, and the cells were obtained dry and sealed. The cells were transferred to a vacuum oven and dried under vacuum at 100 °C overnight (approx. 12 h) to remove any air and moisture from the cell before transferring to an argon filled glovebox. Pouch cells were filled with 0.8 mL of 1.0 M $LiPF_6$ dissolved in a mixture of ethylene carbonate (EC): ethyl methyl carbonate (EMC) in the ratio 3:7 by volume with 2% (by weight) vinylene carbonate (VC) additive (Soulbrain MI) and then sealed at −70 kPa gauge pressure using a vacuum chamber (Audionvac VMS 53, Audion Elektro). A small vacuum is needed to account for vapour pressure of the EMC electrolyte additive. Within 30 min of sealing, cells were held at 1.5 V overnight using a multi-channel battery cycler (BCS-805, Biologic). This avoids dissolution of the copper current collector and gives sufficient time for wetting of the electrodes and separator.

EA-ToF measurements were carried out using an Olympus Epoch 650 ultrasonic flaw detector (Olympus Corp, Japan) with a pulse-echo contact transducer (M110-RM, Olympus Corp, Japan). A frequency of 2.25 MHz was chosen for all EA-ToF measurements using a piezoelectric transducer element (6 mm diameter), capable of frequencies of up to 5 MHz. Ultrasonic couplant (H-2, Olympus Corp, Japan) was applied to maintain interfacial contact between the cell and transducer to facilitate

propagation of the ultrasonic pulse into the pouch cell. Constant pressure was applied behind the transducer with a 200 g weight placed on top of the sensor (Fig. 1). A uniform weight is placed on the transducer to ensure a consistent signal is obtained throughout the measurements. The magnitude of this weight was determined based on the experimental setup to optimise the signal amplitude through the LiB. However, a lower value may be used with a higher initial gain in the acoustic signal to achieve the same results (and vice versa) throughout the measurements, by ensuring consistent contact between the transducer and the cell.

The magnitude of the measured acoustic response by the transducer is in part determined by the gain, which was set at 58 dB to optimise the magnitude of the received signal over the time range of interest. The voltage applied to the piezoelectric transducer was 200 V. The resolution of each waveform data sample, with 8000 discrete mapping points equally spaced across the range of 20 μs, provides a ToF resolution of 20.2 ns for each data point. The ultrasound waveform data was transferred from the Epoch 650 through an RS232 connection and output files acquired by a custom python code. All acoustic data collected was analysed using Python 3.7.

Electrochemical testing was carried out using an SP-200 potentiostat (BioLogic, France). Pouch cells were initially put through a formation cycle using a constant current protocol with an applied rate of C/20 and a potential window of 2.5 V–4.3 V for one cycle. The applied current was based on the nominal capacity of the cells (210 mAh). After initial cycling, pouch cells were disconnected and returned to the glovebox, degassed and resealed for C-rate dependency testing, and acoustic data was collected during cell cycling.

Cells were cycled at room temperature. The cell's external temperature was recorded by attaching two K-Type thermocouples to the bottom surface of the cell (Fig. 1) and temperature was logged using a TC-08 thermocouple interface (PicoTech, U.K.) and PicoLog software (PicoTech, U.K.).

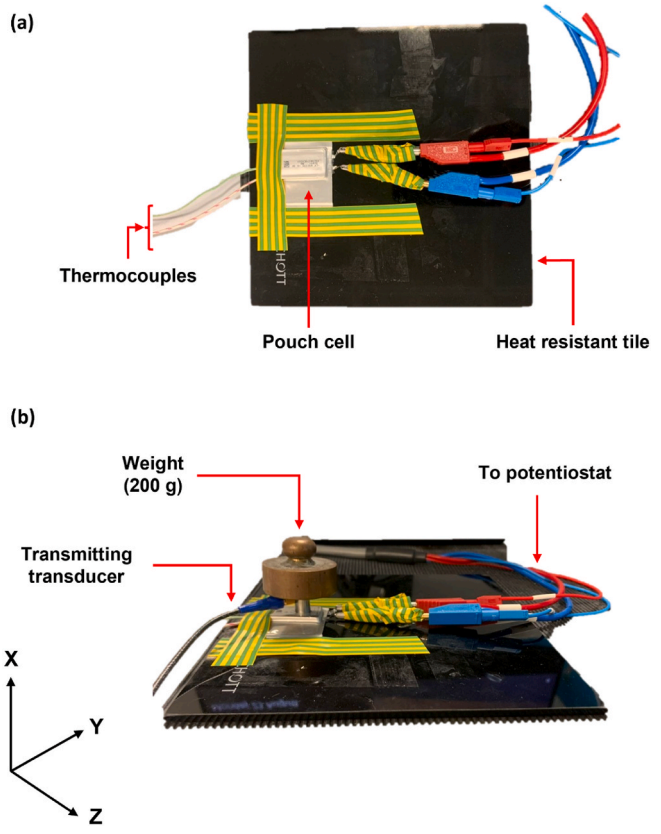

Fig. 1. A photograph of an EA-ToF spectroscopy test set up with a pouch cell top-view (a) and side-view with an ultrasound transducer and weight (b).

A Nikon XTH 225 ST laboratory X-ray microscope was used to probe the internal cell structure of each SC-NMC811/Gr and PC-NMC811/Gr pouch cell before electrochemical cycling. These scans were obtained at an accelerating voltage of 180 kV and an incident beam power of 18.5 W, using a W target and a 0.5 mm Cu filter. 3176 projections were obtained for each scan with the geometric magnification of the system resulting in a pixel size of approximately 24.5 μm "Nikon CT Agent" software was used to reconstruct all radiographic images using a cone beam filtered back projection algorithm. Visualisation of all reconstructed X-ray imaging scans was performed using Avizo software (FEI, France). The software allows for visualisation of all the electrode layers and current collection tabs inside the cell.

To provide electrode morphology information, nano-CT was performed on pristine (uncycled) samples of SC-NMC811 and PC-NMC811 electrodes. An A Series/Compact Laser Micromachining System (Oxford Lasers, Oxford, UK) with a 532 nm wavelength laser was used to prepare samples for nano-CT [19]. Tomographic scans were performed using an Ultra 810 X-ray instrument (Zeiss Xradia 810 Ultra, Carl Zeiss., CA, USA) equipped with a rotating Cr anode source producing a quasi-monochromatic beam with a characteristic emission peak at 5.4 KeV (Cr–Kα). X-ray CT scans were carried out with an X-ray source tube voltage of 30 kV_p with exposure time of 60 s per projection image, and a total of 1001 projection images were collected. All radiographic data reported have isotropic voxel lengths of 126 nm. All reconstructions were achieved using commercial software employing parallel-beam filtered-back-projection (FBP) algorithms ("Reconstructor Scout-and-Scan", Carl Zeiss., CA, USA). 3D visualizations of reconstructed tomograms were processed using Avizo software (FEI, France) which allows particles to be separated and identified. A thresholding algorithm derived from Otsu's method [20] was adopted for segmentation of the NMC particles using the Auto-Threshold module in Avizo [21]. Neighbouring particles that were in contact with one another were separated using the Separate Objects Avizo module which identifies boundaries (lines) between objects and separates them along these boundaries using a 3D watershed algorithm on the segmented binarized image stack [21]. This module also assigns a unique label to each separated object. The Label Analysis Avizo module, was then used to extract volumetric PSD, particle sphericity and surface area. Histograms were plotted for each data range using 24 bins and fitted with Gaussian curves to determine cumulative frequency. The standard deviation and mean values were tabulated for each plotted histogram and correspond to the peak of the Gaussian curves. Border particles were effectively removed from the 3D volume rendering of electrodes using "border kill" function for volumetric PSD analysis, ensuring any subsequent analysis was conducted only on particles that were wholly within the field of view of the imaging. The Volume Fraction module was used to determine the volume fraction of active material, carbon-binder domain (CBD) and pores of each NMC811 electrode.

3. Results and discussion

3.1. EA-ToF spectroscopy measurements of a SC-NMC811/Gr and a PC-NMC811/Gr cell

Naturally, the acoustic signal response received by the ultrasonic flaw detector can vary considerably depending on the sample under investigation. This is to be expected due to the variation in material interfaces across different tested samples. In this work, all EA-ToF experiments were conducted on the same pouch cell geometry to minimise variations between the tested pouch cells. Fig. 2 explains the acoustic response received by the ultrasonic flaw detector-receiver from a SC-NMC811/Gr pouch cell.

The acoustic amplitude of the reflected peaks in an EA-ToF response are in part determined by the reflection coefficient (R). This coefficient describes the amount of reflection of an incident acoustic wave and is

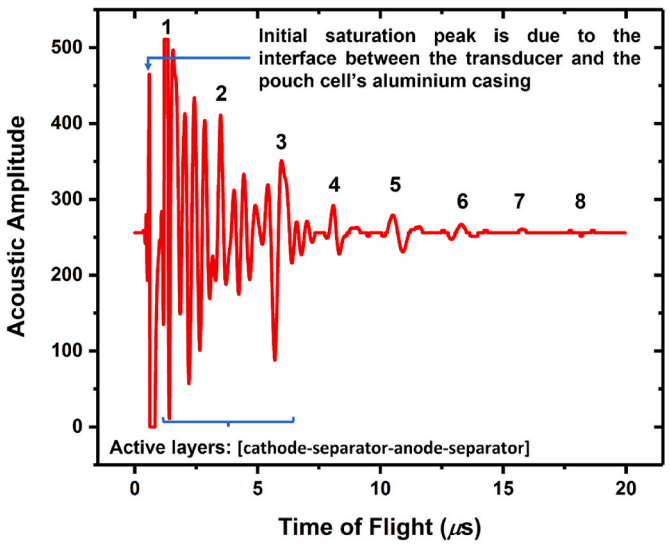

Fig. 2. The initial acoustic waveform generated by pulsing through the layers of a SC-NMC811/Gr pouch cell. Eight 'echo' peaks are identified and annotated as well as the active layers and initial saturation peak due the transducer-pouch cell interface.

highly influenced by the relative acoustic impedance (Z) of the two materials at a given interface [8]. Signal attenuation from the cell will also play a role in the amplitude of the peaks; the deeper the acoustic signal propagates into a cell, the more material the signal has to pass through, so the more attenuated it is and the lower the amplitude of the peak caused at each material interface [22]. The acoustic impedance and reflection coefficient can be calculated as shown in Eqs. (3) and (4). [8]:

$$Z = \rho c \tag{3}$$

$$R = \left(\frac{Z_2 - Z_1}{Z_1 - Z_2}\right)^2 \tag{4}$$

Typically, numerous material flaws such as inter- and intra-particle cracking are expected to alter the ensemble electrode morphology and thus appear on the EA-ToF spectrogram within the peaks associated with the active layers (where an active layer consists of the combination of cathode-separator-anode-separator), for example dampening in acoustic amplitude or intermittent loss of acoustic signal. Gas/SEI formation can cause non discriminative signal attenuation for numerous active layers in the cell simultaneously. The initial acoustic ToF response (Fig. 2) contains several key features that are present throughout all acoustic experiments presented in this work. Firstly, a sharp peak is present at approximately 0.63 μs. This peak is associated with the generation of an ultrasonic pulse. This peak was in the same location for all SC-NMC811/Gr and PC-NMC811/Gr pouch cells measured and was thus treated as an artefact of the signal response [6,10,22]. The following peaks are indicative of the internal structure of the cell. Each peak indicates an interface in the sample, in this case an active layer in the pouch cell [22]. As the ultrasonic sound waveform penetrates deeper through the pouch cell, the amplitude of the signal decreases. This decay in acoustic signal is expected as a result of numerous physical phenomena acting on the sound waveform including wave spreading, signal attenuation and acoustic waves interfering with each other as they pass through the battery medium [10,22]. A portion of the ultrasound propagates through the entire length of the pouch cell and reaches the back wall [23]. This signal is mostly reflected, as opposed to transmitted. This is due to the large difference in acoustic impedance of the air and the pouch cell packaging which results in equally spaced 'echo' peaks that generally have higher acoustic amplitude than other peaks with similar ToF [10,24]. Eight 'echo' peaks can be identified in Fig. 2. The first 'echo' peak (labelled as 1 in Fig. 2) occurs at ~1.5 μs and the final 'echo' peak (labelled as 8 in Fig. 2) occurs at ~18.0 μs. By the time the sound pulse has passed through the active layers and towards the back wall of the pouch cell the signal has dissipated significantly.

The acoustic response of PC-NMC811/Gr and SC-NMC811 cells was monitored for gas formation during their formation cycle because significant gas accumulation is expected as an SEI layer forms on the anode surface [7,25]. EA-ToF measurements were carried out to determine whether the accumulated gas affects the acoustic signal propagating through the cell and in turn effect the EA-ToF response. The cells were then degassed and resealed before continuing acoustic measurements with cell cycling.

The EA-ToF spectrograms plotted with respect to time for the SC-NMC811/Gr and PC-NMC811/Gr cells during formation cycles are shown in Fig. 3 with the red regions representing high amplitude peaks and the blue regions representing low amplitude troughs. White regions correspond to regions where no change in amplitude of the initial generated acoustic pulse is recorded. The first horizonal line at approximately 0.6 μs corresponds to the initial saturation of the transducer and is present in all EA-ToF spectrograms evaluated in this work. The subsequent lines in the EA-ToF spectrograms represent each active layer interface.

Significant acoustic signal attenuation was observed during the first 6 h of cycling of the SC-NMC811/Gr cell and PC-NMC811/Gr cell (see Fig. 3). The gas that forms during SEI formation significantly attenuates the acoustic signal because the impedance mismatch between transducer/gas is higher than for transducer/liquid. A loss of acoustic signal was evident throughout the entire formation cycle; however, most significant signal attenuation occurs during charging, as most electrolyte decomposition occurs at these potentials [26]. The gas that forms on the electrode during SEI formation then diffuses out into other regions of the pouch cell which causes the reappearance of the acoustic signal. The EA-ToF spectrograms collected for the PC-NMC811/Gr cells would suggest that more gas forms during SEI formation in these cells compared to the SC-NMC811/Gr cells (Fig. 3). Signal attenuation due to gas formation perseveres throughout the entire duration of the first charge/discharge cycle to a greater extent than was observed for SC-NMC811/Gr cells.

Once a stable SEI layer has formed, it is expected that cell degradation will occur due to gradual anode passivation, as opposed to the significant gassing that is recorded during the first cycle at C/20 and that LiBs with different anode compositions will exhibit different levels of first cycle signal attenuation [7]. Bommier et al. [7] found that significant gas formation occurs during the first 20 h of a C/20 formation cycle for cells containing silicon-graphite anodes. Therefore, gaseous by-products that arise during SEI formation in silicon anodes are likely to cause acoustic signals to be attenuated differently to silicon-graphite anodes and graphite anodes, respectively. However, these cells have the same anode composition but differing cathode compositions, which implies that differences in first cycle gas evolution caused by different cathode compositions can also be detected with EA-ToF measurements. Whilst the SEI formation principally occurs at the anode, it is established in the literature that there are synergistic effects from anode, cathode and electrolyte that determine the nature of the SEI which are also likely to influence the resultant gassing behaviour [27–29]. As was previously mentioned, SC-NMC811 particles are less likely to have intra-particle cracks compared to PC-NMC811 particles [2]. As in the case of inter-particle cracks, intra-particle cracks are associated with additional electrolyte decomposition, new cathodic SEI layer formation, gas evolution and aggravated electrochemical resistance [30]. There are various reports that suggest more gas evolution occurs in cells that contain PC-NMC811 electrodes compared to SC-NMC811 electrodes [31,32]. Li *et* al. [32] carried out a detailed in-situ gas evolution comparison between SC-NMC811 and Al-coated PC-NMC811 electrodes. The results revealed that PC-NMC811 electrodes release more gas than SC-NMC811 electrodes. In fact, SC-NMC811 electrodes were also found to release negligible gas at 4.6 V. In addition, whilst O_2 release from

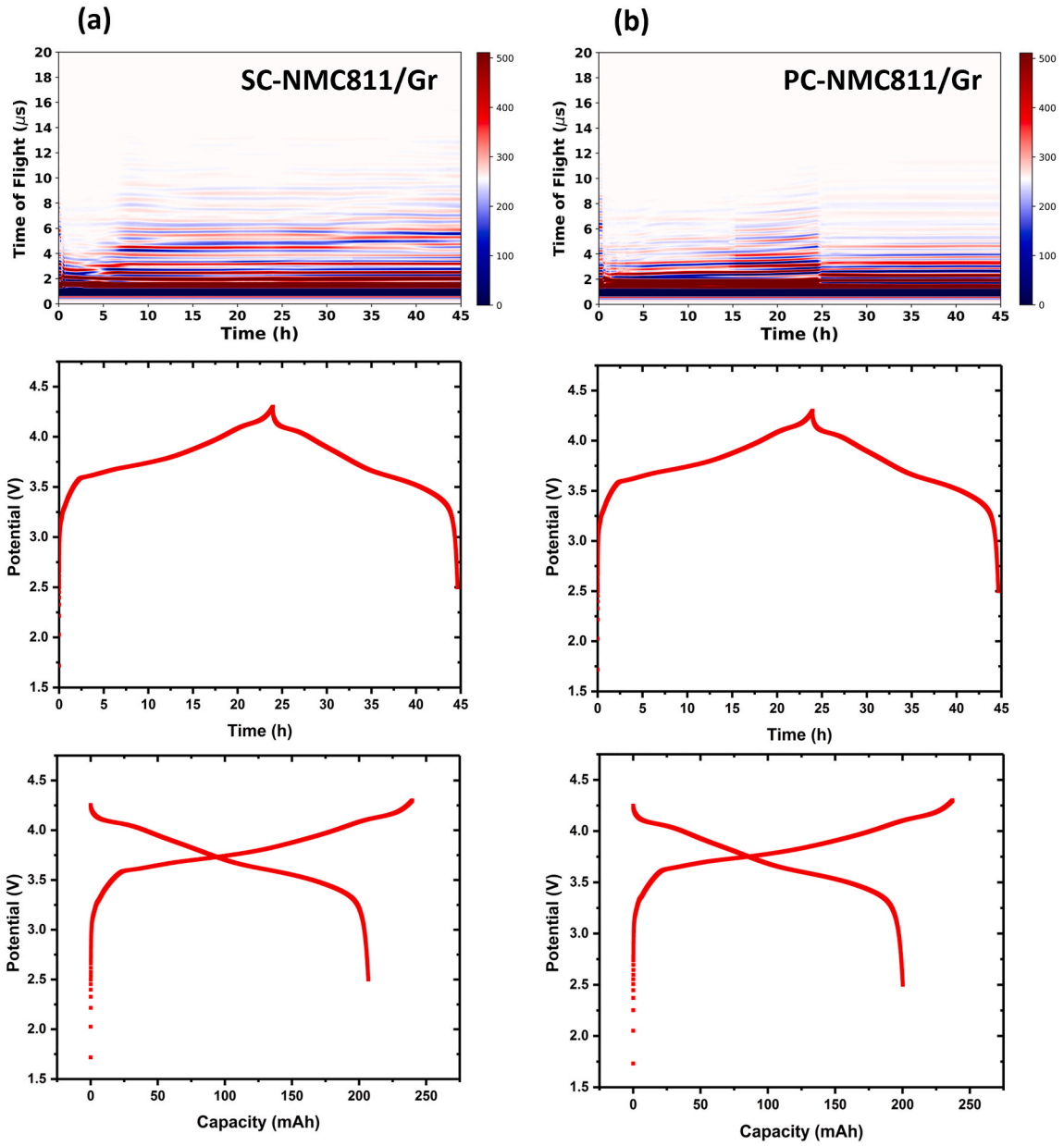

Fig. 3. (a) EA-ToF spectrogram plotted with respect to time with the region where most signal attenuation occurs in white (top); potential profile of the first cycle at a current rate of 0.0105 A (C/20) (middle); and potential profile versus capacity (bottom) of SC NMC811/Gr cell (a, left column) and PC-NMC811/Gr cell (b, right column).

NMC was expected to be higher with increasing voltage, SC-NMC811 electrodes showed lower oxygen intensity indicating that less oxygen release occurs in SC-NMC811 compared with Al-coated PC-NMC811 and uncoated PC-NMC811 electrodes at each voltage.

A C-rate dependency test was carried out on both of the NMC811/Gr cells to determine how EA-ToF measurements are affected by changing the current rate and for determining ToF shift patterns during different C-rates. After the SC-NMC811/Gr cells and PC-NMC811/Gr cells had been formed at C/20, they were tested at constant current rates of C/10, C/5, C/2.5 and 1C. The C-rate was brought back to the initial C-rate (C/10) at the end of the experiment.

EA-ToF signals are highly affected by the state of charge (SoC) of the LiB as lithiation can affect the density and Young's modulus of electrodes [9,33]. The effect of SoC on electrode properties such as the Young's modulus (E), density (ρ) and Poisson ratio (υ) which directly affect the speed of sound (c) are shown in Eq. (5) K and G are the bulk and shear moduli respectively (Eqs. (6) and (7)) [34].

$$c = \sqrt{\frac{K + \frac{4}{3}G}{\rho}} \tag{5}$$

$$K = \frac{E}{3(1-2\nu)} \tag{6}$$

$$G = \frac{E}{2(1+\nu)} \tag{7}$$

Acoustic signals change in their maximum amplitude with respect to time, indicating physical change in the corresponding electrode layers. For example, a highly lithiated anode will have a lower material density and be less dense than the same anode with less lithiation [35]. Graphite (C_6) has a density of 2.26 g cm^{-3}, whereas lithiated graphite (LiC_6) has a density of 2.20 g cm^{-3}. Materials with a higher density are expected to be associated with lower acoustic signal amplitudes than materials with

lower density. However, graphite's (C_6) Young's modulus (E) increases from 32 GPa to 109 GPa when it is fully lithiated (LiC_6) [33,34]. A higher Young's modulus causes a higher acoustic signal amplitude. Therefore, properties can have complicated and opposite effects on the acoustic signal, and therefore the implications of the EA-ToF measurements require care in interpretation. The EA-ToF spectrograms obtained for the SC-NMC811/Gr and PC-NMC811/Gr cells during the C-rate dependency test are shown in Fig. 4.

Lower signal attenuation is present in the EA-ToF spectrogram of the SC-NMC811/Gr cell during the C-rate dependency test than during formation (Fig. 4). EA-ToF signals are more distinct for each active layer in the SC-NMC811/Gr cells. This suggests that most gas formation occurred during the initial SEI formation cycle and that a stable SEI layer had been formed before these experiments. It also confirms that gases formed during the formation cycle were effectively evacuated by the cells' degassing after formation, and before conducting the C-rate dependency test. Nonetheless, there are stark differences between the EA-ToF spectrograms of the SC-NMC811/Gr cell and the PC-NMC811/Gr cell. The acoustic amplitude of the active layers reduces significantly after cycling at 1C in the EA-ToF spectrogram of the PC-NMC811/Gr cell, indicating the formation of gas during the C-rate dependency test in the PC-NMC811/Gr, even after the initial formation cycle was completed. A significant difference is shown in acoustic amplitude in the peaks between the first and final waveform for the PC-NMC811/Gr cell. There are large differences in amplitude of acoustic signals for each active layer between the SC-NMC811/Gr and PC-NMC811/Gr cell. This can occur due to the difference in morphology of the electrode compositions, in particular due to electrode density and Young's modulus. Differences in acoustic intensity measured at active layer interfaces arise from differences in the physical properties of the materials at those interfaces [9]. Although the bulk moduli of the anode and cathode change during cycling, the anode composition is the same in both cells and therefore differences in amplitude are considered to be primarily attributed to differences in the cathode layer. Higher amplitude EA-ToF signals are present in the EA-ToF spectrogram for the SC-NMC811/Gr cell compared to the PC-NMC811/Gr cell. This demonstrates the capability of using EA-ToF spectroscopy to identify differences in cells that vary only in the morphology of the cathode. The difference in morphology between SC-NMC811 electrodes and PC-NMC811 electrodes can have direct consequences on the EA-ToF measurements of the NMC811/Gr cells.

3.2. Morphological characterisation

The internal architecture of each SC-NMC811/Gr and PC-NMC811/Gr pouch cell was examined before electrochemical cycling to identify whether differences in acoustic response between these cells could be attributed to differences in cell build rather than the microstructure of the NMC811 electrode.

The X-ray CT datasets shown in Fig. 5 demonstrate the similarity in internal architecture between the SC and PC cells examined in this work. The SC-NMC811/Gr and PC-NMC811/Gr cells each have the same number of wound active layers [cathode-separator-anode-separator] which result in an equal number of internal interfaces at which acoustic reflections can occur in both cell types (Fig. 5(c) and (d)) [22]. There are also no detectable differences in the internal architecture or defects present in either of the SC-NMC811/Gr cell and PC-NMC811/Gr cells, suggesting that differences in acoustic response between the SC-NMC811/Gr cell and PC-NMC811/Gr cell principally arise as a result of differences in the transmission characteristics of the SC-NMC811 and PC-NMC811 cathodes (as the anodes in both instances are the same), caused by the material properties of the NMC811 electrodes. The graphite anode in the SC-NMC811/Gr and PC-NMC811/Gr cells have the same active mass loading (94.8%) and tap density (1.5 g cm^{-3}). Therefore, acoustic signals are not expected to vary between the cells due to differences in these electrodes.

The nickel current collector tab is clearly visible in Fig. 5; possible complications can be caused in the acoustic response of pouch cells by the current collector tabs running through the length of the cell for approximately 15 mm as the transducer is placed at the centre of the cell, and thus the acoustic signal would have to propagate through the respective tabs (Fig. 5(a) and (b)) [10]. It was ensured that the transducer was placed directly in the centre of each cell during EA-ToF spectroscopy to avoid differences in acoustic response between cells caused by the transducer's location along the length of the current collector inside the cell.

Nano-CT imaging was carried out to visualise differences in morphology between pristine SC-NMC811 and PC-NMC811 electrodes and quantitatively analyse whether these differences could influence the acoustic response of the SC-NMC811/Gr and PC-NMC811/Gr cells. As expected, the polycrystalline particles of the PC-NMC811 electrode are far larger than the single crystal particles of the SC-NMC811 electrode (shown in Fig. 5(g) and (h)). As single crystal particles are smaller than the agglomerated PC-NMC811 particles, optimising the size is critical for the single-crystalline particles to maintain rate capabilities similar to those of polycrystalline particles. Research has suggested a median size of 1–4 μm is sufficient to ensure rate capabilities are maintained in SC systems [36]. The equivalent diameter of particles and pores was extracted from the volume rendering of the SC-NMC811 and PC-NMC811 electrodes to better understand the transmitted acoustic signal propagation through the cell during cycling. Particles in the SC-NMC811 electrode range between 0.1 and 3.0 μm in diameter and particles in the PC-NMC811 electrode range between 1 and 13 μm in diameter (Fig. 6(a) and Fig. 6(b)). Furthermore, larger pore diameters are recorded between active material particles in the PC-NMC811 electrode (1.0–7.5 μm) compared to the SC-NMC811 electrode (around 0.1–1.2 μm) (Fig. 6(c) and (d)). This may be because single crystal particles can be more tightly packed into the electrode than the polycrystalline particles due to their smaller size. As a result, a higher solid phase volume fraction and a lower porosity is recorded for the SC-NMC811 electrode (see Table 1).

Consequently, different acoustic amplitudes are recorded for the active layers between these cells. The PC-NMC811/Gr cell showed more attenuation than the SC-NMC811/Gr during cycling and displayed lower acoustic amplitude peaks corresponding to the active layers that are also present in the SC-NMC811/Gr cell. It is expected that the SC-NMC811 electrodes will have a higher Young's modulus than PC-NMC811 electrodes owing to the higher solid phase volume fraction and smaller interstitial distances between particle grains in the SC-NMC811 electrode, which should result in an overall stiffer electrode with higher signal reflectance and therefore higher acoustic amplitude recordings (see Table 1). It is also possible that PC-NMC811 particles themselves have a lower Young's modulus than SC-NMC811 particles due to SC-NMC811 particles having larger grains compared to smaller, more loosely bound agglomerated grains in the PC-NMC811 particle.

The volumetric particle size distributions (PSDs) (Fig. 6(e) and (f)) extracted from the volume renderings of the SC-NMC811 and PC-NMC811 electrodes are very different, correlating with the particle sizes in the horizontal cross sections through the X-ray tomography scans shown in Fig. 5(e) and (f). The single crystal particles range in volume between 0.5 and 600 μm^3 and the polycrystalline (secondary) particles range in volume between 10 and 1000 μm^3. In addition, a higher number of particles is recorded in the SC-NMC811 electrode region of interest (ROI) compared to the number of particles in the PC-NMC811 electrode ROI. Based on these findings, it is expected that acoustic signals will propagate through the SC-NMC811 electrode in a more facile manner than the PC-NMC811 electrode as acoustic signals propagate through solid media with less attenuation than liquid media (electrolyte), which will fill the interstitial sites in a working cell [37]. Solid media that is higher in density will reduce ToF and increase signal attenuation – in this case, the changes caused by different elastic moduli are far more significant than those caused by the material density as

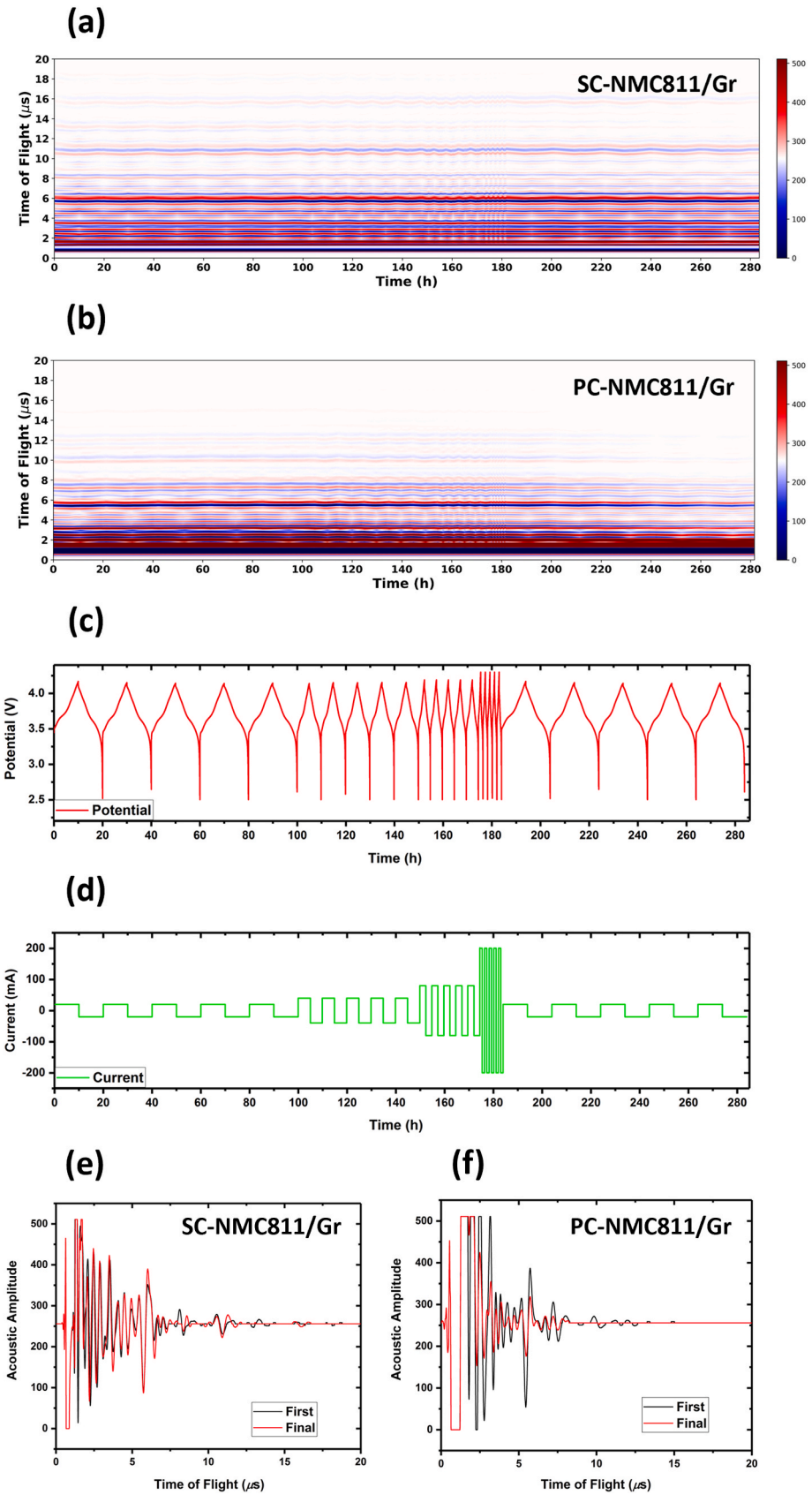

Fig. 4. EA-ToF spectrograms plotted with respect to time for the SC-NMC811/Gr cell (a) and the PC-NMC811/Gr cell (b) during the C-rate dependency test. The potential profile (c) and current profile (d) plotted with respect to time for the SC-NMC811/Gr cell and the PC-NMC811/Gr cell during the C-rate dependency test along with their respective first and final acoustic waveforms received by the ultrasonic flaw detector (e).

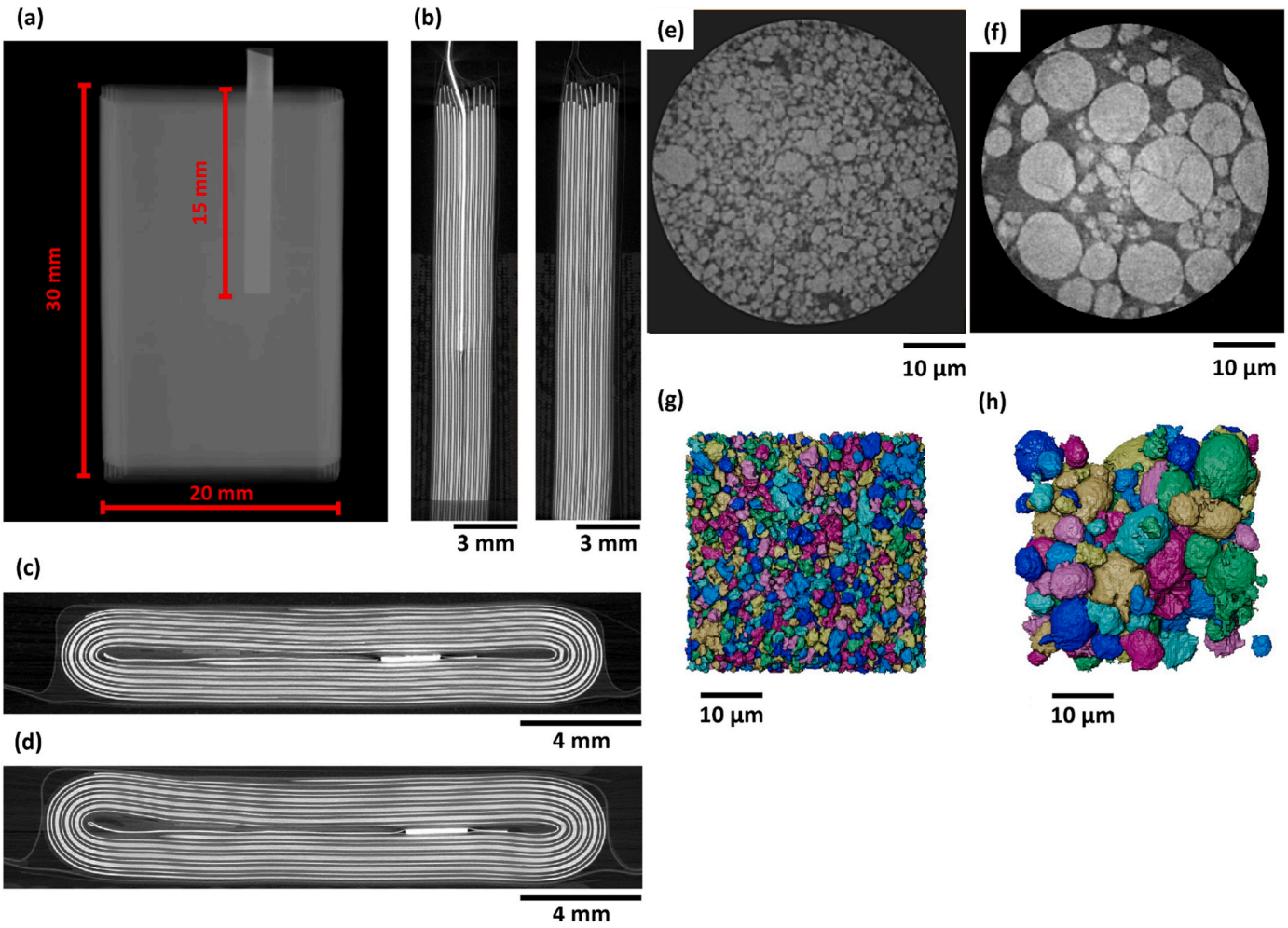

Fig. 5. X-ray CT images of the SC-NMC811/Gr pouch cell showing (a) the volume rendering of the entire cell in the XY plane with the anode current collecting tab, (b) X-ray CT orthogonal slices taken in the XZ plane with the anode current collecting tab present and after the anode current collector tab. X-ray CT renderings of a pristine SC-NMC811/Gr cell (c) and a pristine PC-NMC811/Gr cell (d). Horizontal cross sections through a nano-CT scan of an SC-NMC811 electrode (e) and PC-NMC811 electrode (f). 3D volume rendering of the active material particle network of the SC-NMC811 electrode (g) and PC-NMC811 electrode (h) after reconstruction and segmentation and with a border kill operation applied. Particles are randomly coloured to assist in visualisation.

more signal attenuation is recorded for the PC-NMC811/Gr cell.

The shape factor (or sphericity) characterises how closely a particle resembles a sphere. A particle that has a shape factor of 1 is perfectly spherical with smaller values indicating less sphericity [38]. The shape factor, S, of a particle with a volume of V and surface area of A can be calculated from Eq. (2):

$$S = 6\sqrt{\pi}\,\frac{V}{\sqrt{A^3}} \tag{2}$$

The polycrystalline particles of the PC-NMC811 electrode consist of numerous SC-NMC811 particles agglomerated into larger spherical secondary particles (see Fig. S1) [39]. The SC-NMC811 electrode features a more diverse array of particle shapes and sizes than the PC-NMC811 electrode (Fig. 6(g) and (h)). Nonetheless, the differences in particle shapes between the SC-NMC811 electrodes and PC-NMC811 electrodes are not expected to influence the degree of reflection of the incident acoustic signal because the particles are smaller than the incident acoustic signal wavelength [34]. For instance, when passing through air $\lambda = 70$ µm, aluminium $\lambda = 1200$ µm and copper $\lambda = 452$ µm. The acoustic signal wavelength changes according to the material interface it passes through due to differences in material density and Young's modulus. Therefore, differences in density/morphology between the PC-NMC811 and SC-NMC811 electrodes will cause a difference in acoustic signal wavelength as it passes through these electrodes. Particle size and shape affect material properties of the electrode layer such as electrode density, which alters the signal's wavelength, affect ToF and signal attenuation [40]. Theoretically speaking, it is possible to detect morphological changes such as particle cracking by increasing the frequency of the acoustic signal and thereby shortening its wavelength. However, there is a trade-off as lower ultrasonic frequencies provide better wave penetration through an entire LiB cell, whereas higher frequency provides higher resolution and focal sharpness [5].

The particle surface area and particle volume specific surface area (VSSA) were obtained from the reconstructed microstructure of each NMC811 electrode (Fig. 6(i–l)). VSSA can provide both structural and cycling performance-related information for LiB electrodes, as the particle-pore interface is where charge transfer reactions occur during battery cycling between the active material and the electrolyte. There are large differences in VSSA between particles in the SC-NMC811 electrode and PC-NMC811 electrode. The SC NMC particles have a larger VSSA despite particles in the PC-NMC811 electrode having surface areas ~7 times larger than the largest surface areas in the SC-NMC811 electrode. However, the majority of SC and PC NMC particles have surface areas below 100 µm^2. On average, the SC NMC particles have a smaller surface area than the PC NMC particles. However, polycrystalline particles have been found to crack extensively during cycling, which increases the surface area of the ensemble electrode and provides more sites for Li intercalation/deintercalation [2]. In contrast,

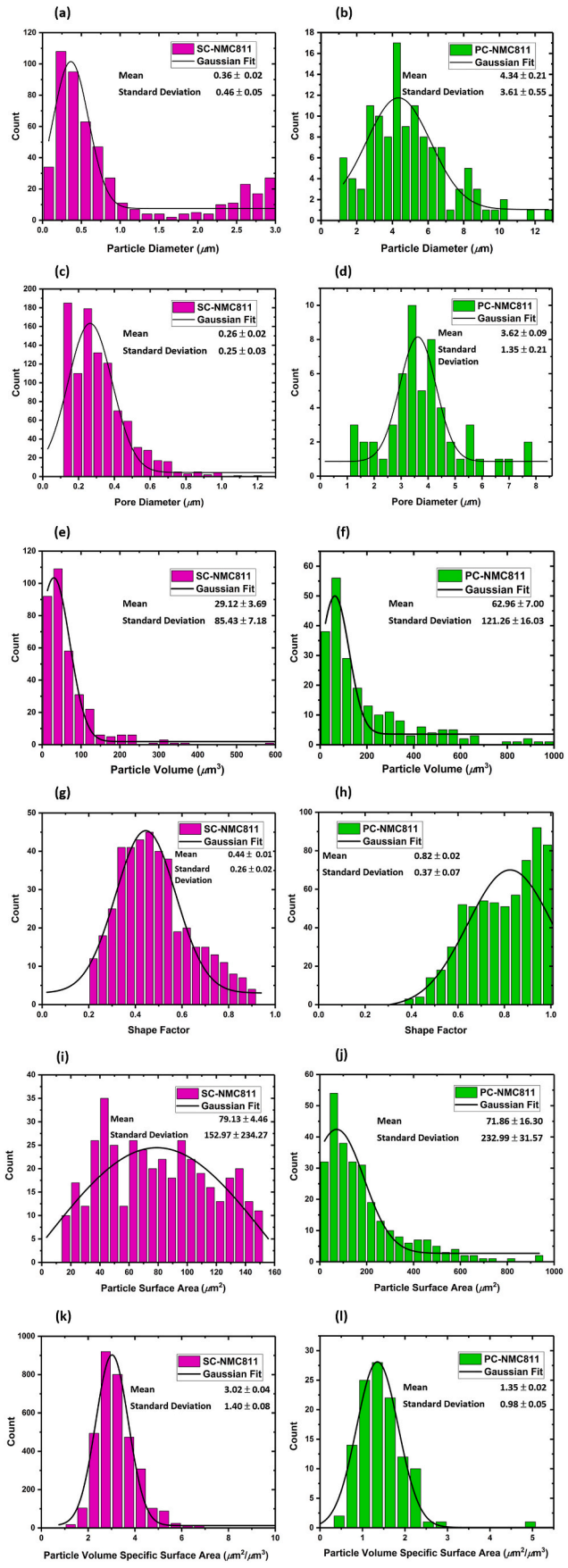

(caption on next column)

Fig. 6. Equivalent particle diameter and pore diameter for the SC-NMC811 electrode (a) and (c) and PC-NMC811 electrode (b) and (d). Volumetric particle size distribution (PSD) of electrode particles in the SC-NMC811 electrode (e) and PC-NMC811 electrode (f). Shape factor (or sphericity) of particles in the SC-NMC811 electrode (g) and PC-NMC811 electrode (h). The surface area of particles in the SC-NMC811 electrode (i) and PC-NMC811 electrode (j). The volume specific surface area of particles in the SC-NMC811 electrode (k) and the PC-NMC811 electrode (l).

single crystal particles do not undergo cracking during cycling [3,41,42]. Therefore, more gas formation and capacity fading occurs in the PC-NMC811/Gr cell during repeated cycling [32,43–46].

Heenan et al. [2] report that various polycrystalline NMC811 particles undergo cracking prior to cycling owing to calendering of the electrode during electrode processing stages. This gives rise to various individual smaller secondary particles that originate from larger particles. These findings suggest that the wider variety of particle surface areas that exist in the PC-NMC811 electrode may be caused by particle cracking which occurred during calendering (see Fig. 6(j)). Both SC-NMC811 and PC-NMC811 electrodes were calendered, which would further suggest that calendering is more detrimental for polycrystalline electrodes. Particle cracking is not expected to occur in the SC-NMC811 electrode to the same degree as the PC-NMC811 electrode owing to their initial size and lack of internal grains (Fig. 6(e)). Larger particles are also more prone to cracking during expansion/contraction of the electrode after repeated charge/discharge cycling leading to various degradation mechanisms such as phase transformation [47], cathode-electrolyte parasitic reactions [48–50] and transition metal dissolution [51,52]. Manganese dissolution from NMC electrodes has been reported to induce elevated rates of electrolyte reduction at the graphite electrode, causing further SEI formation reactions [53]. The gas evolution caused by these reactions would exacerbate signal attenuation.

3.3. Electrochemical characterisation

Fig. 7 indicates that the SC-NMC811/Gr cell underwent minimal capacity loss during the C-rate dependency test. The SC-NMC811/Gr cell has better rate capability as more capacity fading occurs in PC-NMC811/Gr cells compared to SC-NMC811/Gr cells as C-rate is increased (Fig. 7 (c) and (d)). Nonetheless, as expected, neither cells experience significant capacity fading after 20 cycles, suggesting that no deleterious degradation processes are incurred due to higher C-rate cycling for the relatively low number of cycles conducted in this experiment. This observation is reinforced by the absence of changes in the acoustic amplitude of the active layers when the cells are cycled at different C-rates. In fact, the acoustic amplitude measured for each respective electrode layer remains fairly consistent throughout cycling in the NMC811/Gr cells. Measured amplitude is governed by physical changes in the electrode interfaces and intrinsic physical properties. Therefore, it is likely that the different microstructural properties of the SC-NMC811 and PC-NMC811 cathodes cause different degrees of cell polarisation and therefore ionic resistance in the tested cells. The PC-NMC811/Gr cells appear to have higher polarisation than the SC-NMC811/Gr cell as lower capacities are measured at higher C-rates for the PC-NMC811/Gr cell.

According to Fig. 7(e), the highest dQ/dV peak occurs for the slowest charge/discharge cycle (C/10). The height of this peak is similar for all subsequent C-rates including for the cycle that returns to C/10. The dQ/dV curve at 1C is significantly more shifted to higher voltages than the dQ/dV curves for the other C-rates. Charging at increasing C-rates produces the same information, as evidenced by the same shape of the dQ/dV curve; however, the IR-drop is higher at faster C-rates and thus the peak positions appear more shifted [54]. Shifting of dQ/dV curves is also evidence of capacity fade, which agrees with the fall in capacity shown in Fig. 7(b). However, the cell voltage is largely determined by the cathode potential, as opposed to the anode potential. This presents a

Table 1
Active material and pore and CBD volume fraction recorded for each electrode determined using the Volume Fraction module in Avizo.

Electrode	Active material (vol. %)	Pore and CBD (vol. %)
SC-NMC811	73.2	26.8
PC-NMC811	68.8	31.2

drawback in using a dQ/dV plot for full cell systems because peaks are caused by changes in the overall cell voltage, which is the difference between the anode and cathode potentials. Therefore, processes that occur at the anode are more difficult to discern [55,56].

3.4. ToF shift measurements of a SC-NMC811/Gr cell and a PC-NMC811/Gr cell

The 1D displacement of a material interface causes the acoustic signal to pass through the material at a different time during its flight, causing an apparent ToF shift. A negative ToF shift means the acoustic signal travels faster through the cell i.e., a shorter duration of time elapses before the acoustic signal encounters the material interface in question. A positive ToF shift means the acoustic signal takes longer to travel through the cell. This method can be used to track changes in density and Young's modulus during cycling [5]. When the material properties remain constant, a positive ToF shift can correspond to cell expansion, as a thicker cell would ultimately lead to a greater distance through which the ultrasonic wave has to travel. Conversely, a negative ToF shift can be attributed to cell contraction [5,7,34]. Fig. 8 shows the ToF shift recorded for the third echo peak of the SC-NMC811/Gr cell and PC-NMC811/Gr cell during the C-rate dependency test and the associated exterior cell temperature profiles. ToF shift is normalised to zero at the start of charge/discharge cycling. The third echo peak was chosen because it is easily identifiable in the acoustic waveform for both SC-NMC811/Gr and PC-NMC811/Gr cells and has a high acoustic amplitude throughout cycling. The first and second echo peaks also have a high acoustic amplitude but have ToF values that are similar to the active layers in the cell, making it more difficult to isolate during data processing. Nonetheless, all echo peaks represent the signal that has

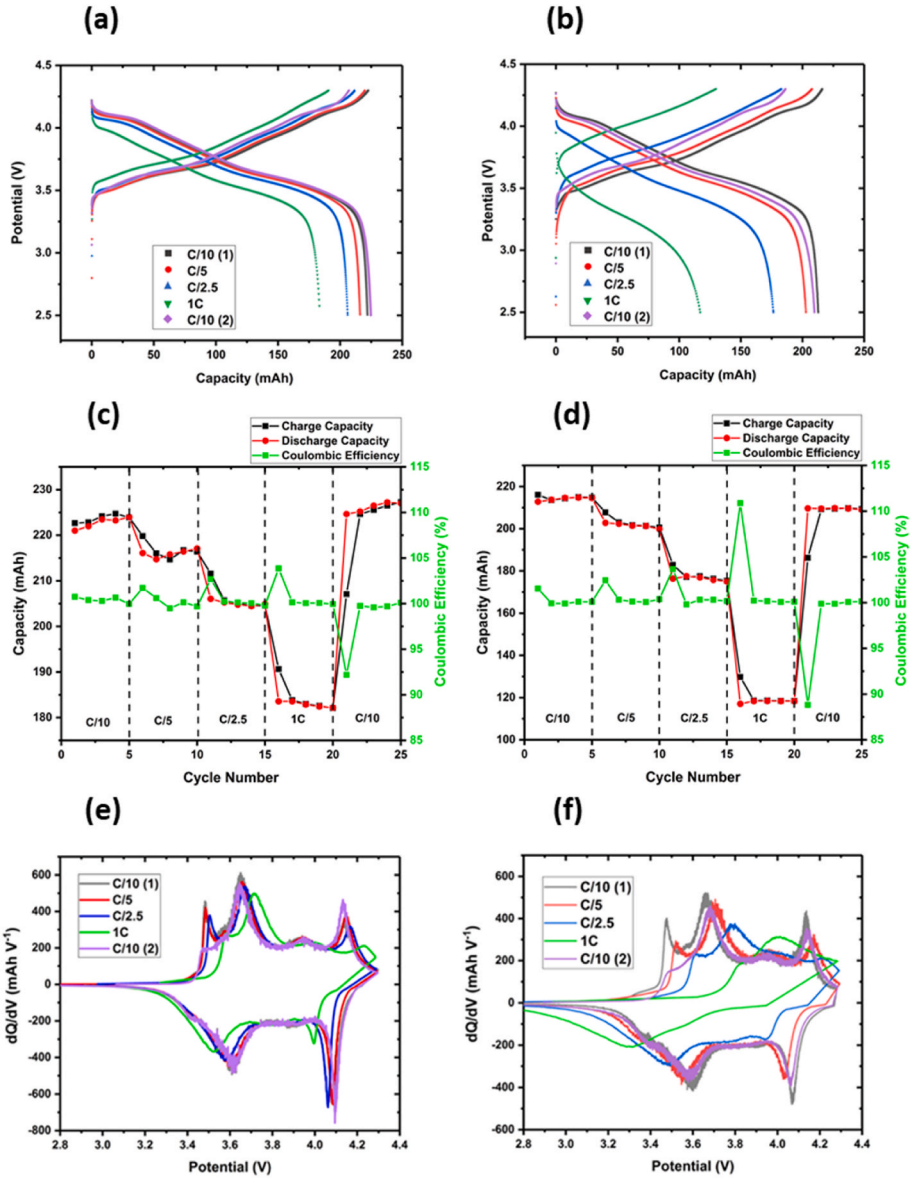

Fig. 7. Electrochemical characterisation for each cell during the C-rate dependency testing: Potential vs capacity plot at each C-rate for the SC-NMC811/Gr cell (a) and PC-NMC811/Gr cell (b), Charge, and discharge capacity and coulombic efficiency vs cycle number for all C-rates for the SC-NMC811/Gr cell (c) and the PC-NMC811/Gr cell (d) and differential capacity vs cell potential curves for the first cycle at each C-rate for the SC-NMC811/Gr cell (e) and PC-NMC811/Gr cell (f).

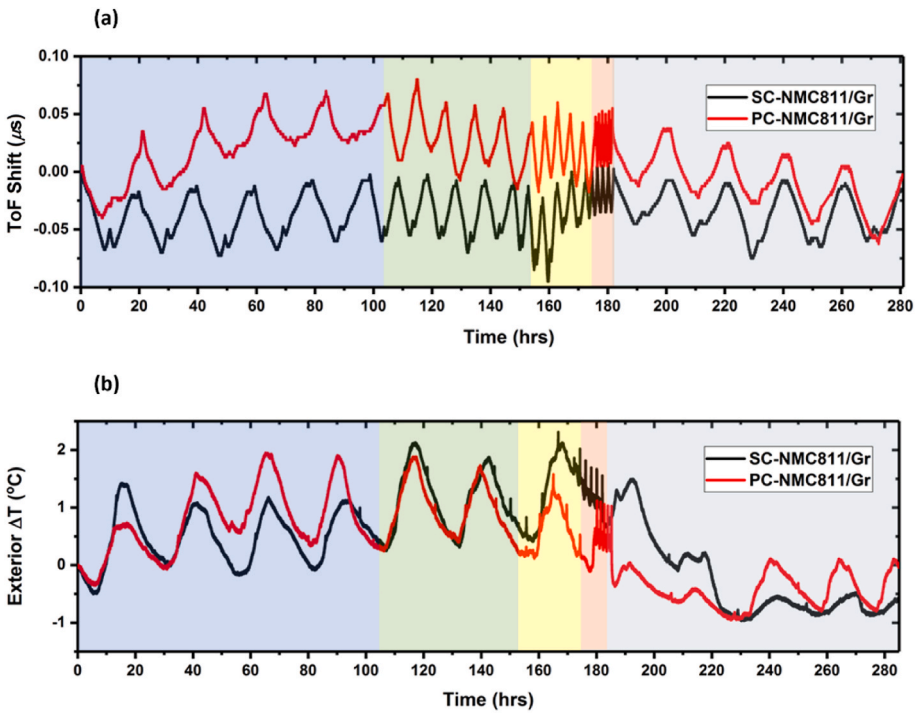

Fig. 8. ToF shift obtained at current rates of C/10, C/5, C/2.5 and 1C for the SC-NMC811/Gr (black) and PC-NMC811/Gr cell (red) (a). (b) The exterior cell temperature during C-rate dependency testing for the SC-NMC811/Gr cell (black) and PC-NMC811/Gr cell (red). Shaded areas in each graph indicate each C-rate: C/10 (blue), C/5 (green), C/2.5 (yellow), 1C (red) and the second C/10 cycling stage (grey). (For interpretation of the references to colour in this figure legend, the reader is referred to the Web version of this article.)

travelled through the entire cell and is reflected back. Therefore, these echo peaks give the same information as each other about the cumulative properties of all the layers within the cell. Other peaks are related to reflections from active layers within the cell and thus will only show changes occurring in those respective layers before the reflection occurs from the back wall of the cell.

ToF shift and acoustic amplitude of peaks are highly influenced by thickness changes of the cell, as well as the interaction between material properties such as electrode density, Young's modulus and electrolyte viscosity, which can also impact ToF shift and acoustic amplitude, resulting in a complex decoupling process of the acoustic signal interaction with the cell [57,58]. For instance, in Fig. 8, during charging a negative ToF shift is observed; if ToF shift was solely attributed to thickness changes, a positive ToF shift would be expected during the first charge at C/10, as lithiation of the graphite anode would cause these electrodes to get thicker. This trend in ToF shift during first charging is due to other material properties playing a confounding role on the ToF shift. Stage 1 corresponds to fully lithiated graphite (LiC_6 stoichiometry) which results in an increase in the Young's modulus of graphite which in turn causes a negative ToF shift according to Eq. (1) [7,34]. In this case, graphite expands ~8% when charging, but the modulus changes by *ca.* ~300%, as such material property changes are dominant [59,60]. NMC811 electrodes only undergo ~2% volume expansion [59,61,62]. This increase in Young's modulus of the graphite electrode increases wave propagation speed and ultimately causes a negative ToF shift. Similar results were reported in acoustic studies conducted by Bommier et al. [7], Ladpli et al. [63] and Knehr et al. [64]. Rong Xu et al. [65] reported that NMC electrodes undergo a decrease in Young's modulus and stiffness during Li extraction from the layered crystalline particles due to Jahn-Teller distortion, depletion of electrostatic interactions of Li–O, and charge localization cumulatively weakening ionic TMs-O bonding. To our knowledge, quantitative information on the Young's modulus of PC-NMC811 and SC-NMC811 electrodes has not yet been reported. During charging, Li extraction and the accompanying decrease in Young's modulus of the NMC811 electrode occur during Li intercalation of graphite and the associated increase in Young's modulus of the graphite electrode. Given that a negative ToF shift is recorded during charging, it is evident that changes in Young's modulus of the graphite electrode are larger than changes in the NMC811 electrode.

The PC-NMC811/Gr cell undergoes a positive ToF shift during C/10 cycling, as ToF shift increases above 0 μs and reaches nearly 0.08 μs after the first charge/discharge during C/5 cycling (see Fig. 8(a)). Both cell capacity and ToF shift then decline with increasing C-rate over time [7]. These changes in ToF shift can arise from cumulative changes in stress and strain of the active layers of the cell during repeated cycling. The largest negative ToF shift occurs during the second C/10 cycling stage, as the cell cools despite PC-NMC811/Gr cell capacity returning to 210 mAh which suggests cell cooling plays a confounding role in ToF shift patterns (see Fig. 8(b)). As mentioned in Section 3.2, the PC-NMC811 electrodes has larger interstitial voids than the SC-NMC811 electrode. These interstitial voids can aid in rapid cooling of the PC-NMC811 electrode despite the higher overpotential and ohmic heating, which would explain why cell cooling is more evident in the PC-NMC811/Gr at faster C-rates and the second C/10 cycling stage than the SC-NMC811/Gr cell. It should be noted that although changes in ToF shift occur between cycles, the magnitude of these ToF shifts are very small which suggest that no severe cell degradation or damage have occurred throughout cycling.

The SC-NMC811/Gr cell is largely characterised by a negative ToF shift pattern throughout the entire C-rate dependency test with a maximum ToF shift of 0 μs at 1C. This is most apparent when a C/2.5 C-rate is applied with ToF shift reaching nearly −0.10 μs. The SC-NMC811/Gr cell stays relatively stable around a centre line (~−0.04 μs ToF shift) whereas the PC-NMC811/Gr cell moves away from a stable ToF, potentially indicating expansion, fracture or dislocation of the reflective interfaces inside the PC-NMC/Gr cell [6]. As both NMC/Gr cells contain the same anode composition, the significantly positive ToF shift recorded for the PC-NMC811/Gr cell throughout cycling can be attributed to the PC-NMC811 electrodes. The ToF shift patterns for the SC-NMC811/Gr cell suggests that it undergoes less changes in stress and strain of the active layers between cycles compared to the PC-NMC811/Gr cell. The ToF shift pattern of the SC-NMC811/Gr cell then increases during 1C cycling towards 0 μs ToF shift. It is the general consensus that higher C-rate operation can lead to thermal expansion in LiBs [66,67]. However, as this increase in ToF shift is not also recorded for the PC-NMC811/Gr cell during 1C operation, it is likely that this

trend is attributed to other physical changes in the NMC811 electrodes. The most negative ToF shift value recorded (−0.10 μs) for the SC-NMC811/Gr cell is not correlated with the lowest cell temperature, implying that other physical properties influence the ToF shift pattern recorded for the SC-NMC811/Gr cell. It has been reported that particles in a SC-NMC electrode undergo less cracking and reduced lattice strains compared to particles in a PC-NMC electrode during repeated cycling, resulting in a more ordered, higher density electrode [68,69]. Increased electrode density, higher electrolyte viscosity, and reduced cell thickness would exacerbate a negative ToF shift as the cell is cooled [58,70,71].

ToF shift maxima do not correlate entirely with exterior cell temperature maxima at slower C-rates. This is expected given the ohmic heating of Li-ion cells during slower CC cycling (slower heating of the cell at slower C-rates), except for at 1C when the ohmic heating is high enough to heat up the cell. This means that the fluctuations/peaks and troughs of the ToF measurements at slower C-rates are more attributable to the ambient room temperature than the electrochemistry of the cell and subsequent changes in material properties.

After the C-rate dependency test, both cells return to their original ToF (i.e., 0 μs) suggesting there is no change in cell thickness after cycling and that the thickness changes that occur during cycling are reversible. The trend in ToF shift during each cycle is consistent throughout charge/discharge cycling with a negative ToF shift during graphite lithiation and positive ToF shift with graphite delithiation. There is no evidence of any further degradation mechanisms occurring during cycling that contribute to the ToF shift measurements of the cell at this length-scale. As expected, the intracycle trends in magnitude of ToF shift are similar for both NMC811/Gr cells given that intracycle ToF shift patterns are dominated by the graphite electrodes, present in both cells. Throughout charge/discharge cycling, the cell periodically expands and contracts as the graphite electrode undergoes Li intercalation/deintercalation [62]. The cell could be said to periodically breathe with charge/discharge cycling. During these reversible processes, simultaneous changes in electrode stress and strain occur at the active layers and effect the speed at which the signal passes through the active layers [72]. This demonstrates the usefulness of ToF shift measurements for gathering information on numerous physical changes that occur during cycling LiBs compared to devices such as push-piston dilatometers, thickness gauges and micrometers that are solely designed to measure cell thickness changes [73,74]. However, the use of these devices in tandem with EA-ToF spectroscopy could be useful to discern which ToF measurements can be attributed to thickness changes of the cell, rather than other functional parameters such as Young's modulus and electrode density.

These two cell chemistries are composed of the same graphite electrode, but different NMC811 electrodes. The difference in ToF shift patterns between the SC-NMC811/Gr and PC-NMC811/Gr cells is therefore most likely to be due to the different physical properties of the NMC811 electrodes which directly cause a variation in the Young's modulus of these respective electrodes. However, there are numerous physical processes that can alter the cell's ToF shift, such as external temperature, cell gassing and material properties. The SC-NMC811 and PC-NMC811 electrodes also have different C-rate dependencies, so at a given C-rate the state of lithiation will be different in the two materials – this may also cause some differences in the ToF as the assumed SoC is different for a given point in the cycle. As the SC-NMC811 and PC-NMC811 electrodes have different Young's modulus and density, the acoustic signal will inevitably vary in its interaction with them (refer to Eqs. (5)–(7)). Difference in density and Young's modulus of these electrodes has a direct influence on the ToF shift.

4. Conclusion

For the first time known to the authors, EA-ToF spectroscopy has successfully been used to distinguish between LiBs composed of either SC-NMC811 or PC-NMC811 electrodes. It has been demonstrated that the acoustic behaviour of LiBs is influenced by the morphology of the NMC811 electrodes, with the different particle sizes influencing density and Young's modulus of the cathode. Consequently, acoustic signals propagate through these respective materials with varying reflectance and transmission. Furthermore, differences in acoustic signal attenuation were recorded during formation cycling of the SC-NMC811/Gr and PC-NMC811/Gr cells which was attributed to gas evolution and SEI layer formation. EA-ToF spectrograms indicated that more gas formed throughout the formation cycle in the PC-NMC811/Gr than the SC-NMC811/Gr cell, despite the SC-NMC811/Gr cell having more gas formation at the beginning of first charging and both cells containing the same anode composition. This was likely attributed to additional electrolyte decomposition, new cathodic SEI layers formation, gas evolution and aggravated electrochemical resistance in the PC-NMC811 electrodes. Furthermore, differences in acoustic amplitude of the active layers were recorded for the PC-NMC811/Gr cell and SC-NMC811/Gr during the C-rate dependency test with gas formation present in the PC-NMC811/Gr cell during later cycles. Generally, a lower acoustic amplitude was detected for the majority of active layers in the PC-NMC811/Gr cell compared to the SC-NMC811/Gr cell which was attributed to differences in particle morphology of the NMC811 electrodes.

Use of X-ray CT revealed some interesting aspects of the interior cell architecture of the tested LiBs. For instance, the elongated tabs that run through around half the length of the cell may affect acoustic signal propagation through the cell. Numerous geometrical parameters such as particle sphericity, equivalent particle/pore diameter and volumetric PSD were assessed for each NMC811 electrode. The PC-NMC811 electrode was largely characterised as having much larger particles with larger interstitial distances between active particles. The SC-NMC811 electrode had far smaller particles, with smaller interstitial distances between them. These differences were hypothesised to influence electrode density and Young's modulus, both critical physical properties that can alter EA-ToF recordings for either material.

Finally, ToF shift patterns revealed differences between cells that vary in particle morphology of the NMC811 cathode. For instance, the PC-NMC811/Gr cell largely underwent positive ToF shifts during C-rate testing whilst the SC-NMC811/Gr cell predominately underwent negative ToF shift during cycling. Nonetheless, an interchanging positive/negative ToF shift was recorded between charge/discharge for the SC-NMC811/Gr cell and PC-NMC811/Gr cells before both returned to their original ToF. Whilst there are numerous physical processes that can affect EA-ToF spectroscopy measurements, it is a powerful technique for measuring physical changes in ostensibly similar cells and using other techniques such as X-ray CT alongside EA-ToF spectroscopy can improve our understanding of cell architecture, and electrode morphology by revealing intrinsic physical attributes that can directly impact EA-ToF measurements.

CRediT authorship contribution statement

H. Michael: Conceptualization, Methodology, Investigation, Formal analysis. **R.E. Owen:** Investigation, Software, Visualization, Formal analysis. **J.B. Robinson:** Methodology, Formal analysis. **T.M.M. Heenan:** Investigation, Formal analysis. **C. Tan:** Sample procurement and preparation. **A.J. Wade:** Investigation. **R. Jervis:** Methodology, Formal analysis, Supervision, Funding acquisition. **D.J.L. Brett:** Conceptualization, Supervision, Funding acquisition. **P.R. Shearing:** Conceptualization, Methodology, Supervision, Funding acquisition.

Declaration of competing interest

The authors declare the following financial interests/personal relationships which may be considered as potential competing interests: Paul. R Shearing reports financial support was provided by The Faraday

Institution. Paul R. Shearing reports financial support was provided by Royal Academy of Engineering. Paul. R Shearing reports financial support was provided by Engineering and Physical Sciences Research Council.

Acknowledgements

This work was supported by The Faraday Institution (faraday.ac.uk; EP/S003053/1), grant number FIRG001, FIRG014, FIRG024; and The Royal Academy for Engineering CiET1718\59. Access to the lab-based X-ray instrument was supported through EP/N032888/1.

Appendix A. Supplementary data

Supplementary data to this article can be found online at https://doi.org/10.1016/j.jpowsour.2022.231775.

References

[1] A. Väyrynen, J. Salminen, J. Chem. Thermodyn. 46 (2012) 80–85.
[2] T.M.M. Heenan, A. Wade, C. Tan, J.E. Parker, D. Matras, A.S. Leach, J.B. Robinson, A. Llewellyn, A. Dimitrijevic, R. Jervis, P.D. Quinn, D.J.L. Brett, P.R. Shearing, Adv. Energy Mater. 10 (2020), 2002655.
[3] G. Liu, M. Li, N. Wu, L. Cui, X. Huang, X. Liu, Y. Zhao, H. Chen, W. Yuan, Y. Bai, J. Electrochem. Soc. 165 (2018) A3040–A3047.
[4] R. Weber, C.R. Fell, J.R. Dahn, S. Hy, J. Electrochem. Soc. 164 (2017) A2992–A2999.
[5] J.O. Majasan, J.B. Robinson, R.E. Owen, M. Maier, A.N.P. Radhakrishnan, M. Pham, T.G. Tranter, Y. Zhang, P.R. Shearing, D.J.L. Brett, J. Phys. Energy 3 (2021), 032011.
[6] M.T.M. Pham, J.J. Darst, D.P. Finegan, J.B. Robinson, T.M.M. Heenan, M.D.R. Kok, F. Iacoviello, R. Owen, W.Q. Walker, O.V. Magdysyuk, T. Connolley, E. Darcy, G. Hinds, D.J.L. Brett, P.R. Shearing, J. Power Sources 470 (2020), 228039.
[7] C. Bommier, W. Chang, J. Li, S. Biswas, G. Davies, J. Nanda, D. Steingart, J. Electrochem. Soc. 167 (2020), 020517.
[8] J.B. Robinson, R.E. Owen, M.D.R. Kok, M. Maier, J. Majasan, M. Braglia, R. Stocker, T. Amietszajew, A.J. Roberts, R. Bhagat, D. Billsson, J.Z. Olson, J. Park, G. Hinds, A. Ahlberg Tidblad, D.J.L. Brett, P.R. Shearing, J. Electrochem. Soc. 167 (2020), 120530.
[9] A.G. Hsieh, S. Bhadra, B.J. Hertzberg, P.J. Gjeltema, A. Goy, J.W. Fleischer, D. A. Steingart, Energy Environ. Sci. 8 (2015) 1569–1577.
[10] J.B. Robinson, M. Maier, G. Alster, T. Compton, D.J.L. Brett, P.R. Shearing, Phys. Chem. Chem. Phys. (2018).
[11] C. Bommier, W. Chang, Y. Lu, J. Yeung, G. Davies, R. Mohr, M. Williams, D. Steingart, Cell Reports Phys. Sci. 1 (2020), 100035.
[12] M.M. Kabir, D.E. Demirocak, Int. J. Energy Res. 41 (2017) 1963–1986.
[13] M.G. Boebinger, J.A. Lewis, S.E. Sandoval, M.T. McDowell, ACS Energy Lett. 5 (2020) 335–345.
[14] Y. He, M. Li, Z. Meng, S. Chen, S. Huang, Y. Hu, X. Zou, Mech. Syst. Signal Process. (2021) 148.
[15] X. Lu, A. Bertei, D.P. Finegan, C. Tan, S.R. Daemi, J.S. Weaving, K.B. O'Regan, T.M. M. Heenan, G. Hinds, E. Kendrick, D.J.L. Brett, P.R. Shearing, Nat. Commun. 11 (2020) 1–13.
[16] A. Yermukhambetova, C. Tan, S.R. Daemi, Z. Bakenov, J.A. Darr, D.J.L. Brett, P. R. Shearing, Sci. Rep. 6 (2016) 1–9.
[17] D. Patel, J.B. Robinson, S. Ball, D.J.L. Brett, P.R. Shearing, J. Electrochem. Soc. 167 (2020), 090511.
[18] C. Tan, A.S. Leach, T.M.M. Heenan, R. Jervis, D.J.L. Brett, P.R. Shearing, in: Y. Gao, W. Song, J.L. Liu, S. Bashir (Eds.), Adv. Sustain. Energy Policy, Mater. Devices, Springer International Publishing, Cham, 2021, pp. 513–544.
[19] J.J. Bailey, T.M.M. Heenan, D.P. Finegan, X. Lu, S.R. Daemi, F. Iacoviello, N. R. Backeberg, O.O. Taiwo, D.J.L. Brett, A. Atkinson, P.R. Shearing, J. Microsc. 267 (2017) 384–396.
[20] C. Tan, A.S. Leach, T.M.M. Heenan, H. Parks, R. Jervis, J.N. Weker, D.J.L. Brett, P. R. Shearing, Cell Rep. Phys. Sci. (2021), 100647.
[21] N. Otsu, P.L. Smith, D.B. Reid, C. Environment, L. Palo, P. Alto, P.L. Smith, IEEE Trans. Syst. Man. Cybern. C (1979) 62–66.
[22] R.J. Copley, D. Cumming, Y. Wu, R.S. Dwyer-Joyce, J. Energy Storage (2021) 36.
[23] Y. Wu, Y. Wang, W.K.C. Yung, M. Pecht, Electron 8 (2019).
[24] C.B. Scruby, K.A. Stacey, G.R. Baldwin, C.B. Scruby, H.N.G. Wadley, J.J. Hill, C. B. Scruby, J. C. Collingwood, 1987.
[25] R. Bernhard, M. Metzger, H.A. Gasteiger, J. Electrochem. Soc. 162 (2015) A1984–A1989.
[26] S.J. An, J. Li, C. Daniel, D. Mohanty, S. Nagpure, D.L. Wood, Carbon N. Y. 105 (2016) 52–76.
[27] W.M. Dose, I. Temprano, J.P. Allen, E. Björklund, C.A. O'Keefe, W. Li, B.L. Mehdi, R.S. Weatherup, M.F.L. De Volder, C.P. Grey, ACS Appl. Mater. Interfaces 14 (2022) 13206–13222.
[28] B.L.D. Rinkel, D.S. Hall, I. Temprano, C.P. Grey, J. Am. Chem. Soc. 142 (2020) 15058–15074.
[29] S. Solchenbach, G. Hong, A.T.S. Freiberg, R. Jung, H.A. Gasteiger, J. Electrochem. Soc. 165 (2018) A3304–A3312.
[30] B. You, Z. Wang, F. Shen, Y. Chang, W. Peng, X. Li, H. Guo, Q. Hu, C. Deng, S. Yang, G. Yan, J. Wang, Small Methods 5 (2021) 1–28.
[31] Y. Kim, ACS Appl. Mater. Interfaces 4 (2012) 2329–2333.
[32] J. Li, A.R. Cameron, H. Li, S. Glazier, D. Xiong, M. Chatzidakis, J. Allen, G. A. Botton, J.R. Dahn, J. Electrochem. Soc. 164 (2017) A1534–A1544.
[33] Y. Qi, L.G. Hector, C. James, K.J. Kim, J. Electrochem. Soc. 161 (2014) F3010–F3018.
[34] G. Davies, K.W. Knehr, B. Van Tassell, T. Hodson, S. Biswas, A.G. Hsieh, D. A. Steingart, J. Electrochem. Soc. 164 (2017) A2746–A2755.
[35] R. Mo, X. Tan, F. Li, R. Tao, J. Xu, D. Kong, Z. Wang, B. Xu, X. Wang, C. Wang, J. Li, Y. Peng, Y. Lu, Nat. Commun. 11 (2020) 1–11.
[36] T. Kimijima, N. Zettsu, K. Teshima, Cryst. Growth Des. 16 (2016) 2618–2623.
[37] V. V Kadam, R. Nayak, in: R. Padhye, R. Nayak (Eds.), Acoust. Text., Springer Singapore, Singapore, 2016, pp. 33–42.
[38] A. Haibel, I. Manke, A. Melzer, J. Banhart, J. Electrochem. Soc. 157 (2010) A387.
[39] T. Wang, K. Ren, M. He, W. Dong, W. Xiao, H. Pan, J. Yang, Y. Yang, P. Liu, Z. Cao, X. Ma, H. Wang, Front. Chem. 8 (2020) 1–8.
[40] M. Musiak, Z. S. Li, 2021, 1–5.
[41] G. Qian, Y. Zhang, L. Li, R. Zhang, J. Xu, Z. Cheng, S. Xie, H. Wang, Q. Rao, Y. He, Y. Shen, L. Chen, M. Tang, Z.F. Ma, Energy Storage Mater. 27 (2020) 140–149.
[42] M. Ge, S. Wi, X. Liu, J. Bai, S. Ehrlich, D. Lu, W.K. Lee, Z. Chen, F. Wang, Angew. Chem. Int. Ed. 60 (2021) 17350–17355.
[43] T. Bond, R. Gauthier, A. Eldesoky, J. Harlow, J.R. Dahn, J. Electrochem. Soc. 169 (2022), 020501.
[44] J. Hu, L. Li, Y. Bi, J. Tao, J. Lochala, D. Liu, B. Wu, X. Cao, S. Chae, C. Wang, J. Xiao, Energy Storage Mater. 47 (2022) 195–202.
[45] J. Langdon, A. Manthiram, Energy Storage Mater. 37 (2021) 143–160.
[46] Y. Lu, T. Zhu, E. McShane, B.D. McCloskey, G. Chen, Small 2105833 (2022) 1–10.
[47] J. Li, R. Shunmugasundaram, R. Doig, J.R. Dahn, Chem. Mater. 28 (2016) 162–171.
[48] S. Bak, E. Hu, Y. Zhou, X. Yu, S.D. Senanayake, S. Cho, K. Kim, K.Y. Chung, X. Yang, K. Nam, Appl. Mater. Interfaces 6 (2014) 22594–22601.
[49] R. Jung, M. Metzger, F. Maglia, C. Stinner, H.A. Gasteiger, J. Electrochem. Soc. 164 (2017) A1361–A1377.
[50] J. Li, L.E. Downie, L. Ma, W. Qiu, J.R. Dahn, J. Electrochem. Soc. 162 (2015) A1401–A1408.
[51] M.D. Radin, S. Hy, M. Sina, C. Fang, H. Liu, J. Vinckeviciute, M. Zhang, M. S. Whittingham, Y.S. Meng, A. Van der Ven, Adv. Energy Mater. 7 (2017).
[52] L. Romano Brandt, J.J. Marie, T. Moxham, D.P. Förstermann, E. Salvati, C. Besnard, C. Papadaki, Z. Wang, P.G. Bruce, A.M. Korsunsky, Energy Environ. Sci. 13 (2020) 3556–3566.
[53] B. Rowden, N. Garcia-Araez, Energy Rep. 6 (2020) 10–18.
[54] B. Wu, V. Yufit, Y. Merla, R.F. Martinez-Botas, N.P. Brandon, G.J. Offer, J. Power Sources 273 (2015) 495–501.
[55] M. Dubarry, V. Svoboda, R. Hwu, B.Y. Liaw, Electrochem. Solid State Lett. 9 (2006).
[56] W. M. Dose, C. Xu, P. Grey, M. F. L. De Volder, W. M. Dose, C. Xu, C. P. Grey, M. F. L. De Volder, *Cell Reports Phys. Sci.* n.d., 1, 100253.
[57] M. Yi, F. Jiang, L. Lu, J. Ren, M. Jin, Y. Yuan, Y. Xiang, X. Geng, X. Zhang, X. Han, M. Ouyang, Int. J. Energy Res. (2021) 1–22.
[58] B. Semburg, Nucl. Instruments Methods Phys. Res. Sect. A Accel. Spectrometers, Detect. Assoc. Equip. 604 (2009) 215–218.
[59] H. Michael, F. Iacoviello, T. Heenan, A. Llewellyn, J. Weaving, R. Jervis, D. Brett, P.R. Shearing, J. Electrochem. Soc. 168 (2021), 010507.
[60] Y. Qi, H. Guo, L.G. Hector, A. Timmons, J. Electrochem. Soc. 157 (2010) A558.
[61] F.B. Spingler, S. Kücher, R. Phillips, E. Moyassari, A. Jossen, J. Electrochem. Soc. 168 (2021), 040515.
[62] M. Bauer, J. V Persson, M.A. Danzer, M. Wachtler, H. Stowe, J. Power Sources 317 (2016) 93–102.
[63] P. Ladpli, F. Kopsaftopoulos, F.K. Chang, J. Power Sources 384 (2018) 342–354.
[64] K.W. Knehr, T. Hodson, C. Bommier, G. Davies, A. Kim, D.A. Steingart, Joule 2 (2018) 1146–1159.
[65] R. Xu, H. Sun, L.S. de Vasconcelos, K. Zhao, J. Electrochem. Soc. 164 (2017) A3333–A3341.
[66] K.Y. Oh, J.B. Siegel, L. Secondo, S.U. Kim, N.A. Samad, J. Qin, D. Anderson, K. Garikipati, A. Knobloch, B.I. Epureanu, C.W. Monroe, A. Stefanopoulou, J. Power Sources 267 (2014) 197–202.
[67] P. Mohtat, J.B. Siegel, A.G. Stefanopoulou, ECS Meet. Abstr. 1–21 (2019).
[68] G. Li, Y. Wen, B. Bin Chu, L. You, L. Xue, X. Chen, T. Huang, A. Yu, ACS Sustain. Chem. Eng. 9 (2021) 11748–11757.
[69] Y. Liu, J. Harlow, J. Dahn, J. Electrochem. Soc. 167 (2020), 020512.
[70] P.A. Oliveira, R.M.B. Silva, G.C. Morais, A.V. Alvarenga, R.P.B. Costa-Félix, J. Phys. Conf. Ser. 733 (2016).
[71] K. Nowacki, W. Kasprzyk, Int. J. Thermophys. 31 (2010) 103–112.
[72] J.B. Robinson, M. Pham, M.D.R. Kok, T.M.M. Heenan, D.J.L. Brett, P.R. Shearing, J. Power Sources 444 (2019), 227318.
[73] H. Popp, M. Koller, M. Jahn, A. Bergmann, J. Energy Storage 32 (2020), 101859.
[74] H. Michael, R. Jervis, D.J.L. Brett, P.R. Shearing, Batter. Supercaps (2021) 1–20.